Inorg. Chem. **2004**, *43*, 7648–7655

Oxidative Verdoheme Formation and Stabilization by Axial Isocyanide Ligation

Sankar Prasad Rath, Marilyn M. Olmstead, and Alan L. Balch*

Department of Chemistry, University of California at Davis, One Shields Avenue, Davis, California 95616

Received June 30, 2004

The effect of isocyanides as axial ligands on the formation and stability of verdoheme by oxidation has been examined. The reaction of $\{Fe^{III}(OEPO)\}_2$ with *t*-butyl isocyanide under dioxygen-free conditions results in the formation of $(t\text{-BuNC})_2Fe^{II}(OEPO^{\bullet})$ with an electron paramagnetic resonance at $g = 2.009$ with a peak-to-peak separation of 23.5 G at 4 K. (OEPO is the trianion of octaethyloxophlorin and $OEPO^{\bullet}$ is the radical dianion obtained from OEPO by one-electron oxidation.) Exposure of chloroform solutions of either $(2,6\text{-xylylNC})_2Fe^{II}(OEPO^{\bullet})$ or $(t\text{-BuNC})_2Fe^{II}(OEPO^{\bullet})$ to dioxygen followed by the addition of ammonium hexafluorophosphate results in their transformation into the diamagnetic verdohemes, $[(2,6\text{-xylylNC})_2Fe^{II}(OEOP)](PF_6)$ and $[(t\text{-BuNC})_2Fe^{II}(OEOP)](PF_6)$, yields 68 and 70%, respectively. (OEOP is the anion of octaethyl-5-oxaporphyrin.) The oxidation reactions of $(2,6\text{-xylylNC})_2Fe^{II}(OEPO^{\bullet})$ and $(t\text{-BuNC})_2Fe^{II}(OEPO^{\bullet})$ have also been monitored by ^1H NMR spectroscopy. No resonances due to paramagnetic products could be detected, the reactions appear to result only in the formation of the diamagnetic verdohemes, and the products are not susceptible to further oxidation.

Introduction

Recent work has shown that reaction of ligands with $\{Fe^{III}(OEPO)\}_2$ (OEPO = the trianion of octaethyloxophlorin) can lead to six-coordinate complexes with markedly different electron distributions as seen in Scheme 1.[1,2] Thus, in $(1\text{-MeIm})_2Fe^{III}(OEPO)$ the tetrapyrrole macrocycle is present in the trianionic oxophlorin form, and the metal is found in the Fe(III) oxidation state. With $(2,6\text{-xylylNC})_2Fe^{II}(OEPO^{\bullet})$ ($OEPO^{\bullet}$ is the radical dianion of octaethyloxophlorin.) the ligand is present as a dianionic radical, and the metal exists as low-spin Fe(II). With the aromatic isocyanides as axial ligands, π-back-bonding to these ligands contributes to stabilization of the low-spin Fe(II) state. Several other examples of the radical ligand ($OEPO^{\bullet}$) have been reported. For example, oxidation of $(py)Zn^{II}(OEPOH)$ and $(py)_2Ni^{II}(OEPOH)$ (py = pyridine) with either dioxygen or diiodine produces the stable free radicals, $(py)Zn^{II}(OEPO^{\bullet})$[3] and $(py)_2Ni^{II}(OEPO^{\bullet})$.[4] These radicals produce sharp, unstructured electron paramagnetic resonance (EPR) spectra at $g = 2.00$. Additionally, oxidation of $\{Fe^{III}(OEPO)\}_2$ with bromine produces the highly oxidized complex $BrFe^{III}(OEPO^{\bullet})$, which contains two paramagnetic centers, the ligand radical, and the Fe(III) ion.[5] Somewhat surprisingly, the radical-containing complexes $(py)Zn^{II}(OEPO^{\bullet})$, $(py)_2Ni^{II}(OEPO^{\bullet})$, and $BrFe^{III}(OEPO^{\bullet})$ are unreactive toward dioxygen, yet the biological process of heme degradation requires that the hydroxylated hemes react with dioxygen and undergo oxidative ring opening.

Heme oxygenase is the protein that binds heme and catalyzes its oxidative degradation via the sequence of steps shown in Scheme 2.[6−8] The initial step results in heme hydroxylation and produces a high-spin iron(III) complex. Treatment of this intermediate with carbon monoxide decreases the intensity of the EPR spectrum of this high-spin form, which has $g = 6.07$, 5.71, and 2.000, and produces a new, free-radical-like resonance in the $g = 2.004-2.008$

* Author to whom correspondence should be addressed. E-mail: albalch@ucdavis.edu.

(1) Rath, S. P.; Omstead, M. M.; Balch, A. L. *J. Am. Chem. Soc*. **2004**, *126*, 6379.
(2) For a review of the properties of complexes of the meso-hydroxylated heme or oxophlorin see: Balch, A. L. *Coord. Chem. Rev*. **2000**, *200−202*, 349.
(3) Balch, A. L.; Noll, B. C.; Zovinka, E. P. *J. Am. Chem. Soc*. **1992**, *114*, 3380.
(4) Balch, A. L.; Noll, B. C.; Phillips, S. L.; Reid, S. M.; Zovinka, E. P. *Inorg. Chem.* **1993**, *32*, 4730.
(5) Balch, A. L.; Latos-Grażyński, L.; Noll, B. C.; Szterenberg, L.; Zovinka, E. P. *J. Am. Chem. Soc.* **1993**, *115*, 11846.
(6) Maines, M. D. *Heme Oxygenase: Clinical Applications and Functions*; CRC Press: Boca Raton, FL, 1992.
(7) Ortiz de Montellano, P. R. *Acc. Chem. Res*. **1998**, *31*, 543.
(8) Yoshida, T.; Migita, C. T. *J. Inorg. Biochem*. **2000**, *82*, 33.

10.1021/ic0491433 CCC: $27.50
Published on Web 10/23/2004

Scheme 1

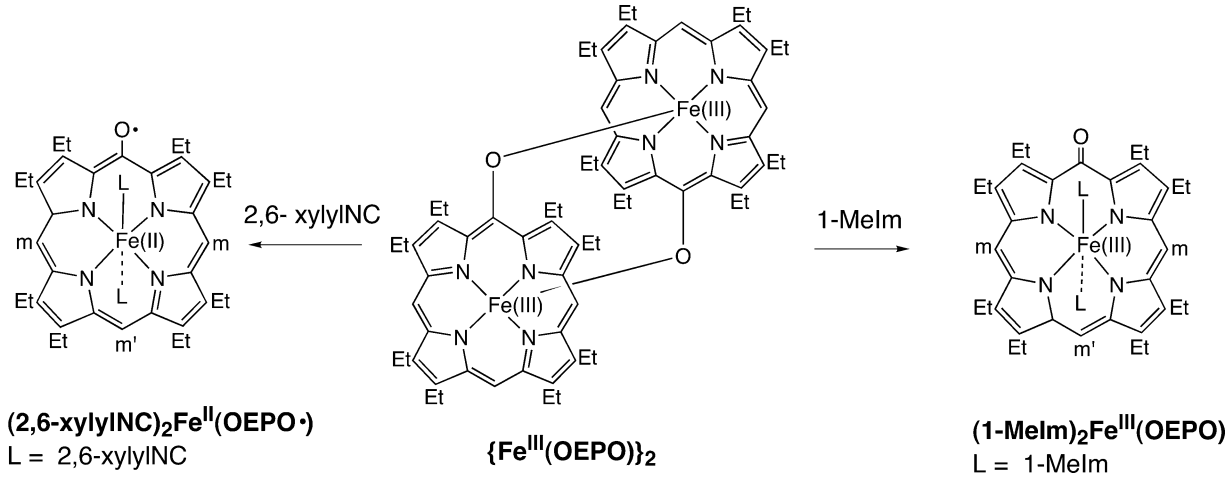

Scheme 2. Heme Oxygenase Activity

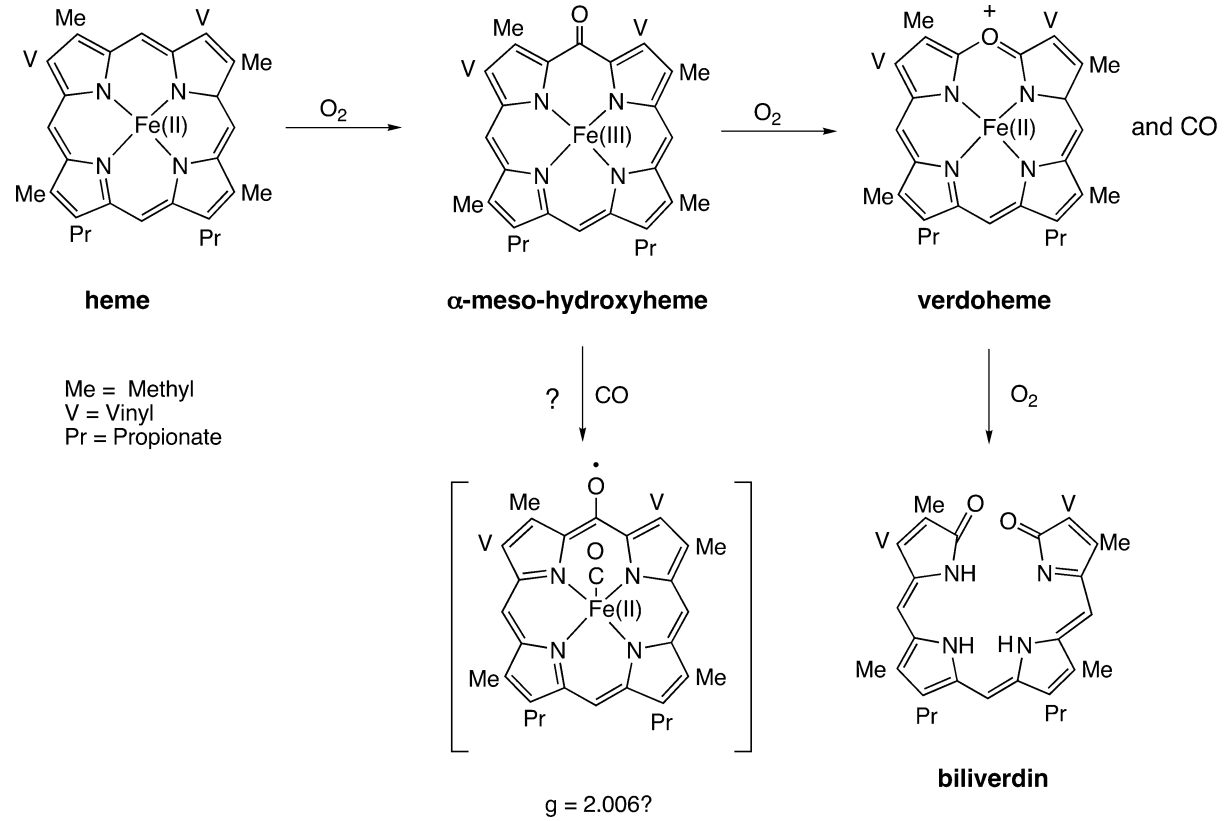

range.[9,10] The observation of an isotropic EPR signal for $(2,6\text{-xylylNC})_2Fe^{II}(OEPO^{\bullet})$ with $g = 2.004$ and a peak-to-peak separation of 24.4 G provides a well-characterized model for the intermediate formed by treatment of the meso-hydroxylated heme bound to heme oxygenase with carbon monoxide. However, attempts to form a corresponding complex with carbon monoxide have led only to the formation of EPR-silent, diamagnetic iron(II) complexes, $(OC)(py)Fe^{II}(OEPOH)$ and $(OC)(N_2H_4)Fe^{II}(OEPOH)$, with one axial carbon monoxide ligand and one axial amine ligand.[11]

Here we further explore the chemistry of isocyanide-ligated intermediates in the heme degradation pathway. We use the alkyl isocyanide, *tert*-butyl isocyanide, to examine the possible effects of further delocalization onto the π-system of the aromatic substituent in 2,6-xylyl isocyanide, and we explore the reactivity of radical-containing complexes such as $(2,6\text{-xylylNC})_2Fe^{II}(OEPO^{\bullet})$ toward further oxidation.

Results

As shown in Scheme 3, treatment of $\{Fe^{III}(OEPO)\}_2$ with *tert*-butyl isocyanide under dioxygen-free conditions also results in the cleavage of the dimer and the formation of

(9) Liu, Y.; Moënne-Loccoz, P.; Loehr, T. M.; Ortiz de Montellano, P. R. *J. Biol. Chem.* **1997**, *272*, 6909.
(10) Sakamoto, H.; Omata, Y.; Palmer, G.; Noguchi, M. *J. Biol. Chem.* **1999**, *274*, 18196.
(11) Rath, S. P.; Olmstead, M. M.; Balch, A. L. *Inorg. Chem.* **2004**, *43*, 6357.

Scheme 3

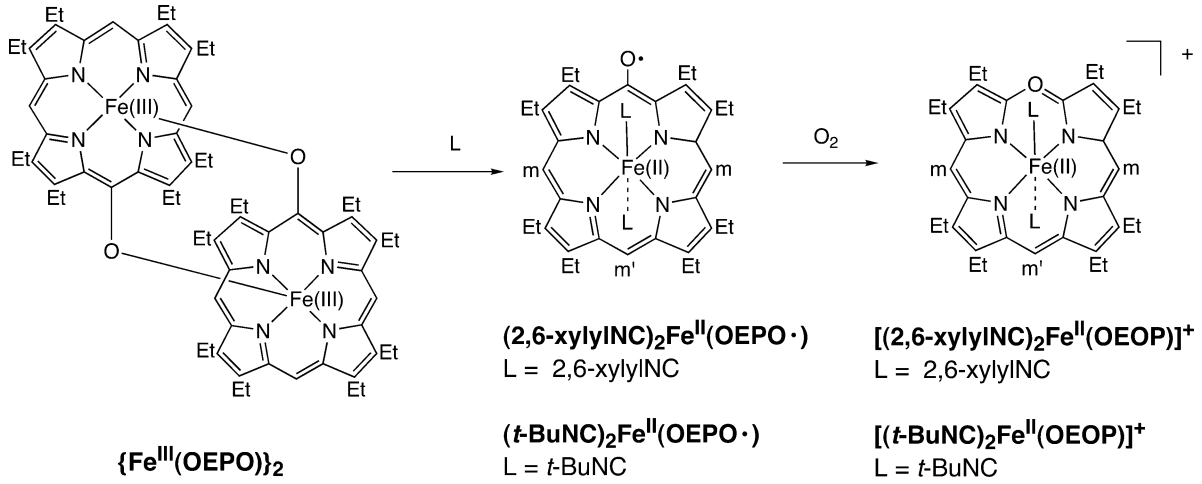

(t-BuNC)$_2$Fe^{II}(OEPO$^{\bullet}$). The latter has been obtained as reddish-black crystals in 56% isolated yield and examined crystallographically as outlined below. A polycrystalline sample of the complex shows an EPR resonance at $g = 2.009$ with a peak-to-peak separation of 23.5 G at 4 K.

Exposure of chloroform solutions of either (2,6-xylylNC)$_2$-Fe^{II}(OEPO$^{\bullet}$) or (t-BuNC)$_2$Fe^{II}(OEPO$^{\bullet}$) to dioxygen followed by the addition of ammonium hexafluorophosphate results in their transformation into the diamagnetic verdohemes [(2,6-xylylNC)$_2$Fe^{II}(OEOP)](PF$_6$) and [(t-BuNC)$_2$Fe^{II}(OEOP)]-(PF$_6$) (OEOP = the anion of octaethyl-5-oxaporphyrin). These salts have been isolated in 68 and 70% yields, respectively. The oxidation reactions of (2,6-xylylNC)$_2$Fe^{II}-(OEPO$^{\bullet}$) or (t-BuNC)$_2$Fe^{II}(OEPO$^{\bullet}$) have also been monitored by ^{1}H NMR spectroscopy. No resonances due to paramagnetic products could be detected; the reactions appear to result only in the formation of the diamagnetic verdohemes. In dichloromethane-d_2 solution, [(2,6-xylylNC)$_2$Fe^{II}(OEOP)]-(PF$_6$) displays ^{1}H NMR resonances at 9.11 and 8.94 ppm in a 2:1 intensity ratio due to the meso protons of the macrocycle, singlets at 6.73 and 6.52 ppm in a 2:1 intensity ratio due to the aromatic protons of the 2,6-xylylisocyanide ligands, a multiplet at 3.60−3.46 ppm due to the methylene resonances, a complex multiplet at 1.72−1.55 ppm due to the methyl groups of the macrocycle, and a sharp singlet at 0.80 ppm due to the methyl groups of the axial ligands. The ^{1}H NMR spectrum of [(t-BuNC)$_2$Fe^{II}(OEOP)](PF$_6$) in chloroform-d solution consists of meso proton resonances at 9.95 and 8.76 ppm in a 2:1 intensity ratio, a complex multiplet at 3.54−3.41 ppm due to the methylene protons, another complex multiplet at 1.70−1.56 ppm due to the methyl groups on the macrocycle, and a singlet at 1.54 ppm due to the *tert*-butyl isocyanide ligands. The UV−vis spectra of [(2,6-xylylNC)$_2$Fe^{II}(OEOP)](PF$_6$) and [(t-BuNC)$_2$Fe^{II}(OEOP)]-(PF$_6$) show typical verdoheme features with intense, low energy absorptions at 632 and 634 nm, respectively. Details are given in the Experimental Section.

Single-Crystal X-ray Structure of (t-BuNC)$_2$Fe^{II}(OEPO$^{\bullet}$). The complex crystallizes with one-half of a molecule in the asymmetric unit with the iron atom located at a center of symmetry. The structure of the molecule is shown in Figure 1. Selected interatomic distances and angles are given in Table 1. The iron is, as expected, six-coordinate, and the Fe−N and Fe−C distances fall in the range expected for iron(II) complexes of porphyrins.

The oxygen atom is disordered with 0.30 occupancy at site O1 and 0.20 occupancy at site O1A. This sort of disorder is frequently found in cases where octaethylporphyrin is

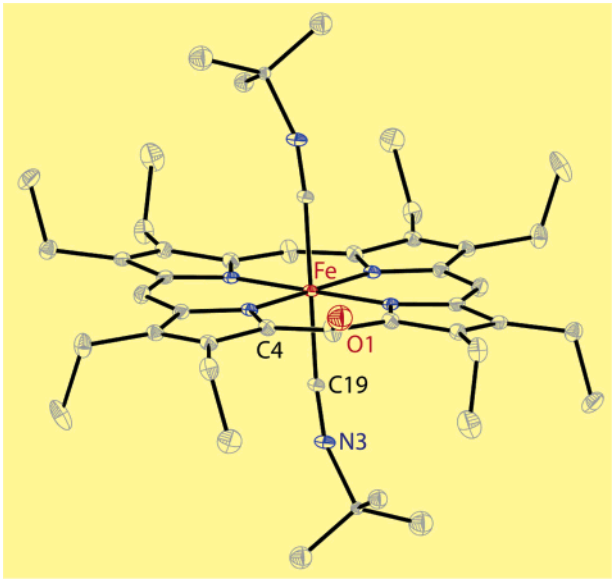

Figure 1. A perspective view of (t-BuNC)$_2$Fe^{II}(OEPO$^{\bullet}$) showing 30% thermal contours.

Table 1. Bond Lengths (Å) and Angles (deg) for (t-BuNC)$_2$Fe^{II}(OEPO$^{\bullet}$)

Bond Lengths			
Fe−N(1)	2.013(3)	N(3)−C(20)	1.541(7)
Fe−N(2)	2.012(3)	N(3)−C(20A)	1.421(10)
Fe−C(19)	1.895(3)	O(1)−C(5)	1.354(14)
N(3)−C(19)	1.157(5)	O(1A)−C(10)	1.37(2)

Bond Angles			
N(1)−Fe−N(2)	89.83(11)	C(19)−Fe−N(2)[a]	83.96(12)
N(1)−Fe−N(2)[a]	90.17(11)	N(3)−C(19)−Fe	168.1(3)
C(19)−Fe−N(1)	93.28(12)	C(19)−N(3)−C(20)	158.3(4)
C(19)−Fe−N(1)[a]	86.72(12)	C(19)−N(3)−C(20A)	160.0(4)
C(19)−Fe−N(2)	96.04(12)		

[a] Symmetry transformations used to generate equivalent atoms: $-x + 1, -y, -z + 1$.

modified by a small substituent attached to one meso carbon atom. For example, the location of the meso-oxygen in {$(py)_2$Fe(OEPO)} is disordered.[12] Other cases of similar disorder are seen in $ClFe^{III}$(*meso*-NC−OEP),[13] Zn^{II}(OEPO•),[2] and (1-MeIm)$_2Fe^{III}$(OEPO).[1] The O1−C5 distance is 1.354(14) Å, and the O1A−C10 distance is 1.37(2) Å.

The Fe−N1 and Fe−N2 distances, which are the in-plane distances to the porphyrin nitrogen atoms, are 2.013(3) and 2.012(3) Å, respectively. The axial Fe−C19 distance is 1.895(3) Å. These distances are similar to those observed for other low-spin iron(II) porphyrins.[14] For comparison the Fe−N distances in (2,6-xylylNC)$_2Fe^{II}$(OEPO•) are 2.0200(12) and 2.0139(12) Å and the axial Fe−C distance is 1.8908(15) Å.[1]

The porphyrin macrocycle in (*t*-BuNC)$_2Fe^{II}$ (OEPO•) is nearly planar, and this observation provides strong evidence that this complex contains Fe(II) rather than Fe(III).[1] Figure 2 shows the displacements of the porphyrin core atoms of (*t*-BuNC)$_2Fe^{II}$(OEPO•) from the plane of the macrocycle and compares those displacements to the corresponding deviations in (2,6-xylylNC)$_2Fe^{II}$(OEPO•). The porphyrin in (*t*-BuNC)$_2Fe^{II}$(OEP) is also nearly planar.[15] In distinct contrast as seen in Figure 5 of ref 1, the Fe(III) complexes, [(*t*-BuNC)$_2Fe^{III}$(OEP)](ClO_4),[16] [(*t*-BuNC)$_2Fe^{III}$(TPP)](ClO_4),[16] and [(2,6-xylylNC)$_2Fe^{III}$(TTP)](CF_3SO_3),[17] have highly distorted, ruffled macrocyclic cores with atomic displacements up to 0.68 Å away from the porphyrin mean plane.

As seen in Figure 3, the C−Fe−C portion of (*t*-BuNC)$_2Fe^{II}$-(OEPO•) is strictly linear because of the crystallographic symmetry, but the Fe−C19−N3 angle (168.1(3)°) is bent as is the neighboring C19−N3−C20 angle (158.3(4)°). This bending of the Fe−C−N−C portion is somewhat greater than the corresponding bending in (2,6-xylylNC)$_2Fe^{II}$(OEPO•) where the C−Fe−C portion is again strictly linear due to crystallographic symmetry, but the Fe−C19−N3 angle (173.17(13)°) and the neighboring C19−N3−C20 angle (169.09(14)°) are displaced from linearity. Similar distortions of isocyanide ligands are seen in (*t*-BuNC)$_2Fe^{II}$(TPP).[15] This sort of displacement from linearity appears to result from packing forces in the solid. As shown in Figure 4, the *t*-Bu groups of neighboring molecules of (*t*-BuNC)$_2Fe^{II}$(OEPO•) abut one another. Bending of the Fe−C−N−C unit alleviates contact between methyl groups on adjacent molecules.

Single-Crystal X-ray Structure of [(*t*-BuNC)$_2Fe^{II}$-(OEOP)](PF$_6$). The complex crystallizes with two independent cations and two anions in the asymmetric unit. There is no crystallographic symmetry imposed on any of the cations or anions. Bond distances and angles are given in Table 2. Figure 5 shows a drawing of one of the six-coordinate iron complexes in the crystal. The other cation is similar as the data in Table 2 show.

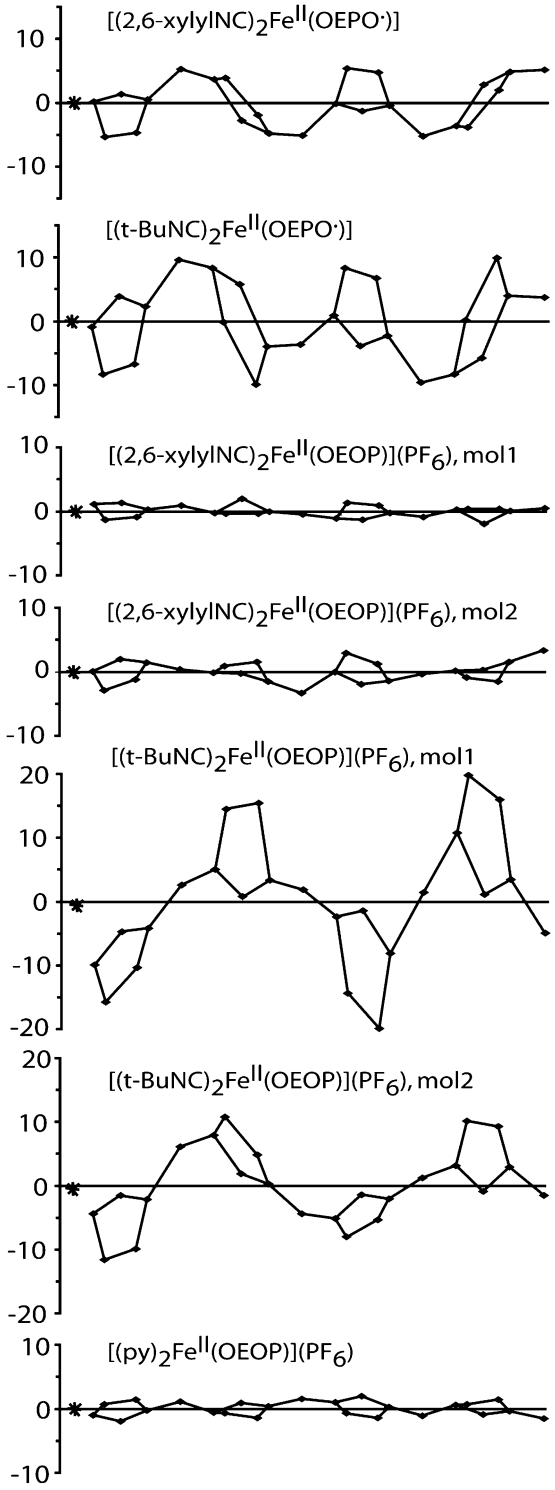

Figure 2. Diagrams showing the out-of-plane displacements of the porphyrin core atoms from the mean plane of the porphyrin for (2,6-xylylNC)$_2Fe^{II}$(OEPO•) (from ref 1), (*t*-BuNC)$_2Fe^{II}$(OEPO•), [(2,6-xylylNC)$_2$-Fe^{II}(OEOP)](PF$_6$)·0.15$CHCl_3$, [(*t*-BuNC)$_2Fe^{II}$(OEOP)] (PF$_6$), and [$(py)_2$-Fe^{II}(OEOP)](PF$_6$) (data from ref 18) in units of 0.01 Å. The positions of the iron atoms are shown by asterisks.

The in-plane Fe−N bond distances in each cation fall into narrow ranges, 1.995(5) to 2.017(5) Å in cation 1 and 1.991(5) to 2.020(5) Å in cation 2. These distances are similar

(12) Balch, A. L.; Koerner, R.; Latos-Grażyński, L.; Noll, B. C. *J. Am. Chem. Soc.* **1996**, *118*, 2760.
(13) Kalish, H.; Camp, J. E.; Stępień, M.; Latos-Grażyński, L.; Olmstead, M. M.; Balch, A. L. *Inorg. Chem.* **2002**, *41*, 989.
(14) Scheidt, R. W.; Reed, C. A. *Chem. Rev.* **1981**, *81*, 543.
(15) Jameson, G. B.; Ibers, J. A. *Inorg. Chem.* **1979**, *18*, 1200.
(16) Walker, F. A.; Nasri, H.; Turowska-Tyrk, I.; Mohanrao, K.; Watson, C. T.; Shokhirev, N. V.; Debrunner, P. G.; Scheidt, W. R. *J. Am. Chem. Soc.* **1996**, *118*, 12109.
(17) Simonneaux, G.; Schünemann, V.; Morice, C.; Carel, L.; Toupet, L.; Winkler, H.; Trautwein, A. X.; Walker, F. A. *J. Am. Chem. Soc.* **2000**, *122*, 4366.

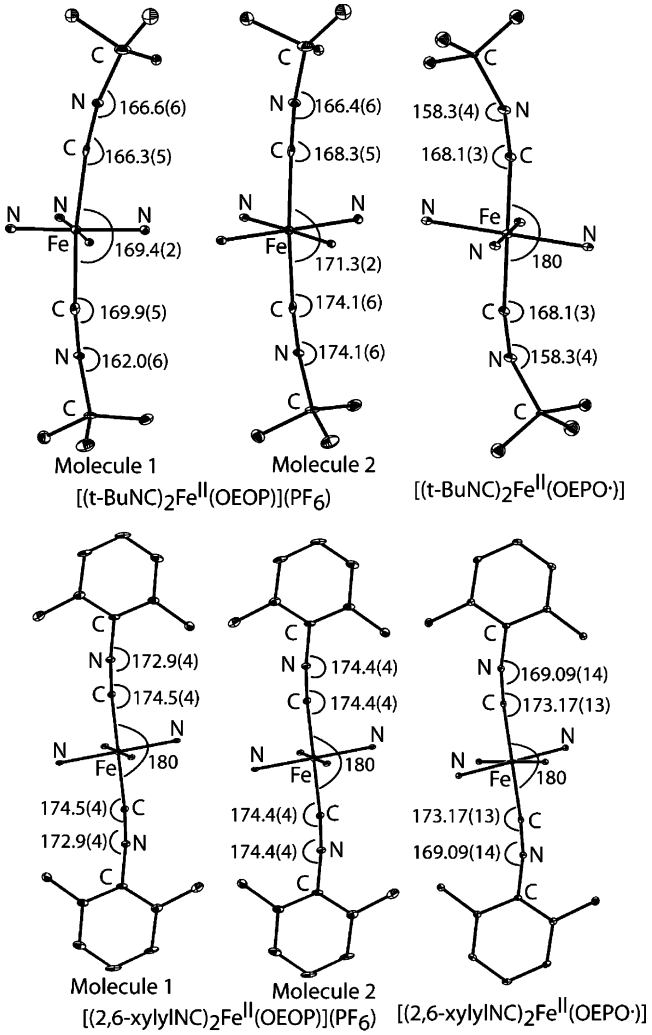

Figure 3. A diagram showing the degrees of bending in the C−N−C−Fe−C−N−C portions of (t-BuNC)$_2$Fe^{II}(OEPO$^{\bullet}$), [(t-BuNC)$_2$Fe^{II}(OEOP)]$^+$, (2,6-xylylNC)$_2$Fe^{II}(OEPO$^{\bullet}$), and [(2,6-xylylNC)$_2$Fe^{II}(OEOP)]$^+$.

to the in-plane Fe−N distances, which range from 1.977(6) to 1.966(5) Å in [(py)$_2$Fe^{II}(OEOP)](PF$_6$).[18] They are also similar in length to those of (t-BuNC)$_2$Fe^{II} (OEPO$^{\bullet}$), which are given in Table 1. The Fe−C bond lengths, 1.925(7) and 1.944(7) Å in cation 1 and 1.938(7) and 1.951(6) Å in cation 2, are somewhat longer than the corresponding Fe−C distances in (t-BuNC)$_2$Fe^{II}(OEPO$^{\bullet}$) (1.895(3) Å) and (t-butylNC)$_2$Fe^{II}(TPP) (1.900(3) and 1.901(3) Å).[15]

As seen in Figure 2, the porphyrins in [(t-BuNC)$_2$Fe^{II}-(OEOP)](PF$_6$) show slight saddle distortions. The effect is much larger in cation 1 than in cation 2. Consequently, it is likely that packing effects are responsible for the distortions.

The C−N−C−Fe−C−N−C portion of each cation is significantly distorted from linearity as the data in Figure 3 show. In contrast to the situation in (t-BuNC)$_2$Fe^{II}(OEPO$^{\bullet}$) where the C−Fe−C portion is required by crystal symmetry to be linear, the C−Fe−C portion of each cation of [(t-BuNC)$_2$Fe^{II}(OEOP)]$^+$ is bent (169.4(2)° in cation 1 and 171.3° in cation 2). Again inspection of the packing in the solid suggests that the bending of the axial ligands allows these units to avoid unusually close contact with the axial ligands on adjacent cations in a manner similar to that seen in Figure 4 for (t-BuNC)$_2$Fe^{II}(OEPO$^{\bullet}$).

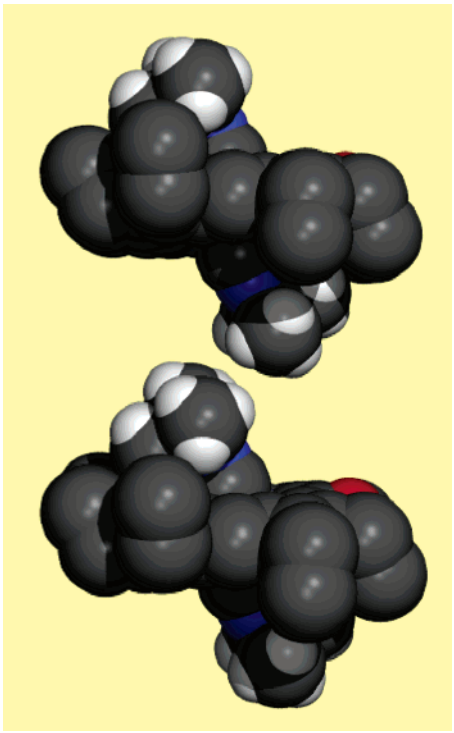

Figure 4. A diagram showing the contacts between two molecules of (t-BuNC)$_2$Fe^{II}(OEPO$^{\bullet}$) and the bending of the isocyanide ligands away from one another. For clarity, protons are shown only on the t-Bu groups of the axial ligands.

Table 2. Bond Lengths (Å) and Angles (deg) for [(t-BuNC)$_2$Fe^{II}(OEOP)](PF$_6$)

cation 1		cation 2	
	Bond Lengths		
Fe(1)−N(1)	1.995(5)	Fe(51)−N(51)	1.991(5)
Fe(1)−N(2)	2.017(5)	Fe(51)−N(52)	2.020(5)
Fe(1)−N(3)	2.003(5)	Fe(51)−N(53)	1.987(5)
Fe(1)−N(4)	2.005(5)	Fe(51)−N(54)	2.004(5)
Fe(1)−C(36)	1.925(7)	Fe(51)−C(86)	1.938(7)
Fe(1)−C(41)	1.944(7)	Fe(51)−C(91)	1.951(6)
O(1)−C(19)	1.367(7)	O(51)−C(69)	1.357(7)
O(1)−C(1)	1.388(7)	O(51)−C(51)	1.383(7)
N(5)−C(36)	1.201(7)	N(55)−C(86)	1.165(7)
N(5)−C(37)	1.488(8)	N(55)−C(87)	1.493(7)
N(6)−C(41)	1.160(7)	N(56)−C(91)	1.184(7)
N(6)−C(42)	1.477(7)	N(56)−C(92)	1.485(8)
	Bond Angles		
N(1)−Fe(1)−N(2)	90.8(2)	N(51)−Fe(51)−N(52)	91.6(2)
N(1)−Fe(1)−N(3)	178.0(2)	N(51)−Fe(51)−N(53)	177.9(2)
N(1)−Fe(1)−N(4)	87.46(19)	N(51)−Fe(51)−N(54)	86.9(2)
N(2)−Fe(1)−N(3)	90.62(19)	N(52)−Fe(51)−N(53)	90.4(2)
N(2)−Fe(1)−N(4)	178.1(2)	N(52)−Fe(51)−N(54)	178.3(2)
N(3)−Fe(1)−N(4)	91.1(2)	N(53)−Fe(51)−N(54)	91.1(2)
C(36)−Fe(1)−N(1)	94.6(2)	C(86)−Fe(51)−N(51)	89.4(2)
C(41)−Fe(1)−N(1)	93.2(2)	C(91)−Fe(51)−N(51)	94.8(2)
C(36)−Fe(1)−N(2)	83.4(2)	C(86)−Fe(51)−N(52)	88.9(2)
C(41)−Fe(1)−N(2)	89.4(2)	C(91)−Fe(51)−N(52)	83.4(2)
C(36)−Fe(1)−N(3)	87.0(2)	C(86)−Fe(51)−N(53)	90.3(2)
C(41)−Fe(1)−N(3)	85.4(2)	C(91)−Fe(51)−N(53)	85.8(2)
C(36)−Fe(1)−N(4)	95.8(2)	C(86)−Fe(51)−N(54)	91.9(2)
C(41)−Fe(1)−N(4)	91.6(2)	C(91)−Fe(51)−N(54)	95.9(2)
C(36)−Fe(1)−C(41)	169.4(2)	C(86)−Fe(51)−C(91)	171.3(2)
N(5)−C(36)−Fe(1)	169.9(5)	N(55)−C(86)−Fe(51)	174.1(6)
C(36)−N(5)−C(37)	162.0(6)	C(86)−N(55)−C(87)	174.1(6)
N(6)−C(41)−Fe(1)	166.3(5)	N(56)−C(91)−Fe(51)	168.3(5)
C(41)−N(6)−C(42)	166.6(6)	C(91)−N(56)−C(92)	166.4(6)

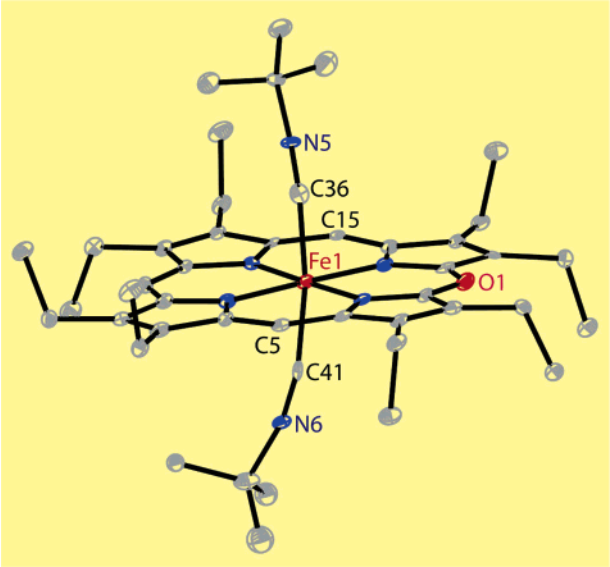

Figure 5. A perspective view of the cation 1 of $[(t\text{-BuNC})_2Fe^{II}(OEOP)]^+$ showing 30% thermal contours.

Table 3. Bond Lengths (Å) and Angles (deg) for $[(2,6\text{-xylylNC})_2Fe^{II}(OEOP)](PF_6)\cdot 0.15CHCl_3$

molecule 1		molecule 2	
	Bond Lengths		
Fe(1)−N(1)	1.974(3)	Fe(51)−N(51)	1.982(4)
Fe(1)−N(2)	1.976(3)	Fe(51)−N(52)	1.978(3)
Fe(1)−C(19)	1.900(4)	Fe(51)−C(69)	1.902(4)
O(1)−C(1)	1.306(14)	O(51)−C(51)	1.302(15)
O(1)−C(9)	1.347(15)	O(51)−C(59)	1.461(19)
N(3)−C(19)	1.154(5)	N(53)−C(69)	1.151(5)
N(3)−C(20)	1.402(5)	N(53)−C(70)	1.399(5)
	Bond Angles		
N(1)−Fe(1)−N(2)	90.13(14)	N(51)−Fe(51)−N(52)	90.19(15)
N(1)−Fe(1)−N(2)[a]	89.87(14)	N(52)−Fe(51)−N(51)[b]	89.81(15)
C(19)−Fe(1)−N(1)	92.52(15)	C(69)−Fe(51)−N(51)	87.31(16)
C(19)−Fe(1)−N(2)	92.26(15)	C(69)−Fe(51)−N(52)	91.92(15)
C(19)−Fe(1)−N(1)[a]	87.48(15)	C(69)−Fe(51)−N(51)[b]	92.69(16)
C(19)−Fe(1)−N(2)[a]	87.74(15)	C(69)−Fe(51)−N(52)[b]	88.08(15)
N(3)−C(19)−Fe(1)	174.5(4)	N(53)−C(69)−Fe(51)	174.4(4)
C(19)−N(3)−C(20)	172.9(4)	C(69)−N(53)−C(70)	174.4(4)

[a] Symmetry transformations used to generate equivalent atoms: $-x+1, -y, -z+1$. [b] $-x+2, -y+1, -z+1$.

Single-Crystal X-ray Structure of $[(2,6\text{-xylylNC})_2Fe^{II}(OEOP)](PF_6)\cdot 0.15CHCl_3$. There are two half-cations in the asymmetric unit. The iron ion in each cation resides on a center of symmetry. Bond distances and angles in the two cations are compared in Table 3. A drawing of one of the cations is shown in Figure 6. The other cation has a similar structure as the data in Table 3 show.

The structure of the cations in $[(2,6\text{-xylylNC})_2Fe^{II}(OEOP)](PF_6)\cdot 0.15CHCl_3$ is similar to those in $[(t\text{-BuNC})_2Fe^{II}(OEOP)](PF_6)$ as the data in Tables 2 and 3 and in Figure 3 show. However, the C−N−C−Fe−C−N−C portion is not as greatly distorted from linearity in $[(2,6\text{-xylylNC})_2Fe^{II}(OEOP)](PF_6)\cdot 0.15CHCl_3$. This can be seen in Figure 3. The presence of a center of symmetry requires that the central C−Fe−C portion is strictly linear. Additionally, the porphyrin in $[(2,6\text{-xylylNC})_2Fe^{II}(OEOP)]^+$ is more nearly planar than it is in either cation of $[(t\text{-BuNC})_2Fe^{II}(OEOP)]^+$. This observation reinforces the suggestion that the saddle distortions seen for both cations in $[(t\text{-BuNC})_2Fe^{II}(OEOP)](PF_6)$ are due to packing effects in the solid.

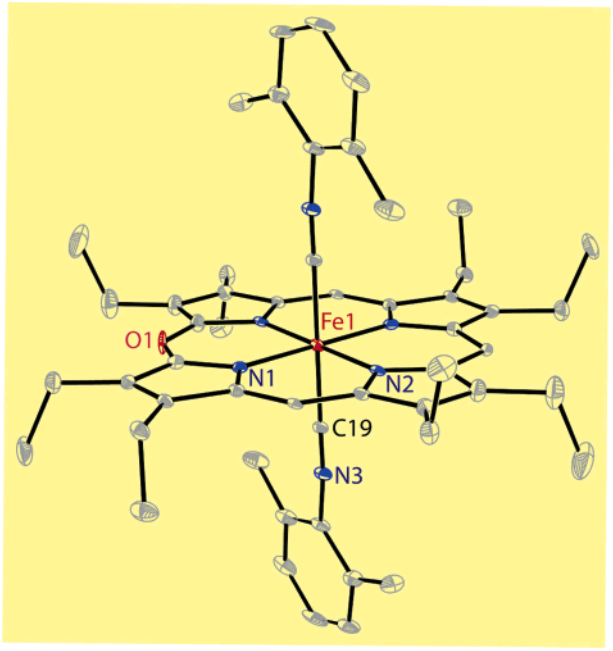

Figure 6. A perspective view of the cation 1 of $[(2,6\text{-xylylNC})_2Fe^{II}(OEOP)]^+$ showing 30% thermal contours.

Discussion

The results presented here show that both aliphatic and aromatic isocyanide ligands react with $\{Fe^{III}(OEPO)\}_2$ to produce six-coordinate products, $(t\text{-BuNC})_2Fe^{II}(OEPO^{\bullet})$ and $(2,6\text{-xylylNC})_2Fe^{II}(OEPO^{\bullet})$, in which the Fe(II) oxidation state is stabilized and the tetrapyrrole ligand is present as a radical dianion. The structural characteristics and the EPR spectra of $(t\text{-BuNC})_2Fe^{II}(OEPO^{\bullet})$ and $(2,6\text{-xylylNC})_2Fe^{II}(OEPO^{\bullet})$ are similar, and these similarities indicate that the presence of an aromatic substituent on the isocyanide ligand does not contribute to the stabilization of the iron(II) electronic ground state.

The complexes $(t\text{-BuNC})_2Fe^{II}(OEPO^{\bullet})$ and $(2,6\text{-xylylNC})_2Fe^{II}(OEPO^{\bullet})$ are reactive toward dioxygen and are smoothly converted into the corresponding verdohemes in relatively high yield. In this regard, $(t\text{-BuNC})_2Fe^{II}(OEPO^{\bullet})$ and $(2,6\text{-xylylNC})_2Fe^{II}(OEPO^{\bullet})$ differ from other radical-containing complexes, $(py)Zn^{II}(OEPO^{\bullet})$,[3] $(py)_2Ni^{II}(OEPO^{\bullet})$,[4] and $BrFe^{III}(OEPO^{\bullet})$,[5] that are stable to exposure to dioxygen.

The oxidations of $(t\text{-BuNC})_2Fe^{II}(OEPO^{\bullet})$ and $(2,6\text{-xylylNC})_2Fe^{II}(OEPO^{\bullet})$ are interesting, because they stop with the formation of the verdohemes, $[(t\text{-BuNC})_2Fe^{II}(OEOP)]^+$ and $[(2,6\text{-xylylNC})_2Fe^{II}(OEOP)]^+$. In contrast, as shown in Scheme 4, oxidation of $(py)_2Fe^{III}(OEPO)$ in pyridine solution initially produces the diamagnetic verdoheme, $[(py)_2Fe^{II}(OEOP)]^+$,[19,20] and the biliverdin complex, $(py)_xFe^{III}(OEB)$.[19,20] Further exposure of verdoheme, $[(py)_2Fe^{III}$-

(18) Balch, A. L.; Koerner, R.; Olmstead, M. M. *J. Chem. Soc., Chem. Commun.* **1995**, 873.
(19) Balch, A. L.; Latos-Grażyński, L.; Noll, B. C.; Olmstead, M. M.; Safari, N. *J. Am. Chem. Soc.* **1993**, *115*, 9056.
(20) St. Claire, T. N.; Balch, A. L. *Inorg. Chem.* **1999**, *38*, 684.

Scheme 4

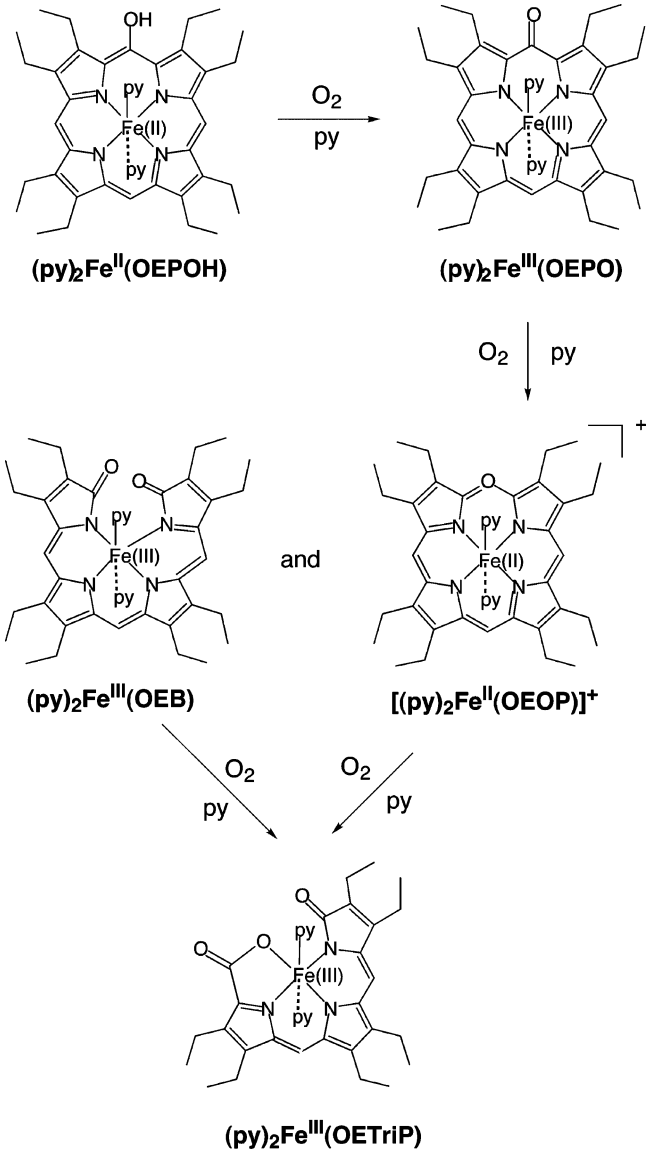

$(OEOP)]^+$, and the biliverdin complex, $(py)_xFe^{III}(OEB)$, to dioxygen produces the tripyrrole complex, $(py)_2Fe^{III}(OETriP)$.[21]

Coupled oxidation involves the oxidation of a heme[19,20] or heme protein[22] by dioxygen in the presence of a sacrificial reducing agent that is usually hydrazine or ascorbic acid. In pyridine solution, coupled oxidation of $(py)_2Fe^{II}(OEP)$ also results in the formation of the verdoheme, $[(py)_2Fe^{III}(OEOP)]^+$, and the biliverdin complex, $(py)_xFe^{III}(OEB)$.[19] In this reaction, the yield of the verdoheme $[(py)_2Fe^{II}(OEOP)]^+$ is only ca. 50%.[19] In a prior study of coupled oxidation by ^{1}H NMR measurements, further oxidation to form the tripyrrole complex, $(py)_2Fe^{III}(OETriP)$, was not observed because of the presence of the reductant or the sluggish nature of the reaction.[20]

The yield of verdoheme in this process is about 42% and thus is lower than that found in the oxidation reactions that form $[(2,6\text{-xylylNC})_2Fe^{II}(OEOP)](PF_6)$ and $[(t\text{-BuNC})_2Fe^{II}(OEOP)](PF_6)$. Coupled oxidation of the H63M mutant of the outer mitochondrial membrane cytochrome b_5 also is arrested at the verdoheme stage and does not go on to produce biliverdin or its iron complex.[23,24] This mutant has the heme present in a hexacoordinate form with axial histidine and methionine ligands. It has been proposed that these axial ligands prevent subsequent binding of dioxygen and thus retard further oxidation. However, coupled oxidation of the H63V mutant of outer mitochondrial membrane cytochrome b_5 (which has a noncoordinating valine replacing the histidine that usually acts as an axial heme ligand) is also arrested after the formation of verdoheme despite the fact that this mutant was designed to provide a vacant coordination site at the heme pocket where dioxygen could enter the verdoheme coordination sphere.[25] Coupled oxidation of a cytochrome b562 mutant that has a five-coordinate iron with an axial methionine to the heme is also restricted to the formation of verdoheme.[26] In examining the reactivity of axial ligand mutants of mitochondrial cytochrome, Rivera and co-workers concluded that the differences in reactivity reflected differences in the mechanism of the initial oxygenation of the heme.[27] It is possible that the high yield of verdoheme formation from $(t\text{-BuNC})_2Fe^{II}(OEPO^{\bullet})$ and $(2,6\text{-xylylNC})_2Fe^{II}(OEPO^{\bullet})$ may result from mechanistic changes in the reaction path that are dependent on the axial ligands present during oxidation. The differences in the ground electronic structures of $(py)_2Fe^{III}(OEPO)$ and $(RNC)_2Fe^{II}(OEPO^{\bullet})$ may result in variations in the mechanisms of their oxidations.

Verdohemes can be converted into iron biliverdin complexes either by hydrolysis[28] or by oxidation.[29] In the present work where the oxidations are conducted in a nonaqueous solvent, the axial isocyanide ligands are acting to prevent the oxidative rather than the hydrolytic reaction. Tight binding of the isocyanide ligands in $[(t\text{-BuNC})_2Fe^{II}(OEOP)]^+$ and $[(2,6\text{-xylylNC})_2Fe^{II}(OEOP)]^+$ may inhibit access of dioxygen to the iron and render the complexes air stable. In contrast, the five-coordinate verdohemes, $ClFe^{II}(OEOP)$ and $BrFe^{II}(OEOP)$, react readily with dioxygen to form an iron−biliverdin complex in an unusually highly oxidized form.[28]

Experimental Section

Materials. Iron(III) octaethylporphyrin chloride was purchased from Mid Century. Samples of $\{Fe^{III}(OEPO)\}_2$ [30] and $(2,6\text{-xylylNC})_2Fe^{II}(OEPO^{\bullet})$[1] were prepared by established routes. All the solvents used were carefully degassed by five freeze/pump/thaw cycles prior to use.

(21) Rath, S. P.; Olmstead, M. M.; Latos-Grażyński, L.; Balch, A. L. *J. Am. Chem. Soc.* **2003**, *125*, 12678.
(22) Hildebrand, D. P.; Tang, H.; Luo, Y.; Hunter, C. L.; Smith, M.; Brayer, G. D.; Mauk, A. G. *J. Am. Chem. Soc.* **1996**, *118*, 12909.
(23) Rodriguez, J. C.; Rivera, M. *Biochemistry* **1998**, *37*, 13082.
(24) Rodriguez, J. C.; Desilva, T.; Rivera, M. *Chem. Lett.* **1998**, 353.
(25) Avila, L.; Huang, H.; Rodriguez, J. C.; Moënne-Loccoz, P.; Rivera, M. *J. Am. Chem. Soc.* **2000**, *122*, 7618.
(26) Rice, J. K.; Fearnley, I. M.; Barker, P. D. *Biochemistry* **1999**, *38*, 16847.
(27) Avila, L.; Huang, H.; Damaso, C. O.; Lu, S.; Moënne-Loccoz, P.; Rivera, M. *J. Am. Chem. Soc.* **2003**, *125*, 4103.
(28) Koerner, R.; Latos-Grażyński, L.; Balch, A. L. *J. Am. Chem. Soc.* **1998**, *120*, 9246.
(29) Nguyen, K.; Rath, S. P.; Latos-Grażyński, L.; Olmstead, M. M.; Balch, A. L. *J. Am. Chem. Soc.* **2004**, *126*, 6210.
(30) Balch, A. L.; Koerner, R.; Latos-Grażyński, L.; Lewis, J. E.; St. Claire, T. N.; Zovinka, E. P. *Inorg. Chem.* **1997**, *36*, 3892.

Table 4. Crystal Data and Data Collection Parameters

	$(t\text{-BuNC})_2Fe^{II}(OEPO^{\bullet})$	$[(t\text{-BuNC})_2Fe^{II}(OEOP)](PF_6)$	$[(2,6\text{-xylylNC})_2Fe^{II}(OEOP)](PF_6)\cdot 0.15CHCl_3$
formula	$C_{46}H_{61}FeN_6O$	$C_{45}H_{61}F_6FeN_6OP$	$C_{53.15}H_{61.15}Cl_{0.45}F_6FeN_6OP$
formula weight	769.86	902.82	1016.80
color and habit	reddish black block	green block	green plate
crystal system	monoclinic	triclinic	monoclinic
T, K	90(2)	90(2)	90(2)
space group	$P2_1/n$	$P\bar{1}$	$P2/c$
a, Å	13.2105(19)	16.848(3)	20.865(5)
b, Å	13.4647(19)	17.691(4)	10.814(3)
c, Å	13.5343(19)	18.896(4)	27.785(5)
α, deg	90	74.64(3)	90
β, deg	117.046(2)	85.91(3)	126.530(12)
γ, deg	90	62.41(3)	90
V, Å^3	2144.1(5)	4804.8(17)	5038(2)
radiation (λ, Å)	Mo Kα (0.71073)	Mo Kα (0.71073)	Mo Kα (0.71073)
Z	2	4	4
d_{calcd}, g cm^{-3}	1.192	1.248	1.341
μ, mm^{-1}	0.392	0.409	0.422
range of transm factors	0.95−0.99	0.96−0.98	0.83−0.98
no. of unique data	3994	46789	10956
no. of restraints	12	36	21
no. of params refined	251	1093	645
R1[a]	0.066	0.099	0.085
wR2[b]	0.198	0.320	0.222

[a] For data with $I > 2\sigma I$. $R1 = \sum||F_o| - |F_c||/\sum|F_o|$. [b] For all data. $wR2 = (\sum[w(F_o^2 - F_c^2)^2]/\sum[w(F_o^2)^2])^{1/2}$.

Preparation of $(t\text{-BuNC})_2Fe^{II}(OEPO^{\bullet})$. Under an atmosphere of purified dinitrogen, 0.50 g (6.0 mmol) of *tert*-butyl isocyanide was added to a suspension of 50 mg (0.043 mmol) of $\{Fe^{III}(OEPO)\}_2$ in 10 mL of dioxygen-free chloroform. The mixture was stirred for 5 min to form a dark brown solution. The resulting solution was filtered to remove any solid residue, and then the volume of the solution was reduced to one-half under reduced pressure. Dioxygen-free *n*-hexane was then carefully layered over the solution in a dinitrogen-filled glovebox. On standing 4 to 5 days, dark red crystals of the products formed: yield 37 mg, 56%. UV−vis spectrum (under a dinitrogen atmosphere) in dichloromethane with 1% *tert*-butyl isocyanide (λ_{max}, nm (ϵ, M^{-1} cm^{-1})): 400 (3.8×10^4), 425 (5.1×10^4), 818 (1.0×10^4). The complex shows an EPR resonance in the solid state at $g = 2.009$ (peak-to-peak separation, 23.5 G) at 4 K.

Preparation of $[(2,6\text{-xylylNC})_2Fe^{II}(OEOP)](PF_6)\cdot 0.15CHCl_3$. A 100 mg (0.116 mmol) sample of $(2,6\text{-xylylNC})_2Fe^{II}(OEPO^{\bullet})$ was dissolved in 100 mL of chloroform and stirred for 1 h in air. The dark red solution turns green during this time. A methanolic solution of ammonium hexafluorophosphate was added to the solution, and the resulting mixture was evaporated to dryness. The residue was redissolved in 10 mL of chloroform. This solution was filtered. A sample of *n*-hexane was layered over the filtrate. Dark, greenish-black crystals were obtained after 3 to 4 days. The crystalline solid was collected by filtration and air-dried: yield 79 mg, 68%. UV−vis spectrum in dichloromethane (λ_{max}, nm (ϵ, M^{-1} cm^{-1})): 370 (3.8×10^4), 414 (2.2×10^4), 530 (1.0×10^4), 584 (1.5×10^4), 632 (4.6×10^4).

Preparation of $[(t\text{-BuNC})_2Fe^{II}(OEOP)](PF_6)$. A 100 mg (0.130 mmol) sample of $(t\text{-BuNC})_2Fe^{II}(OEPO^{\bullet})$ was treated as stated above. The yield of the crystalline product was 82 mg (70%). UV−vis spectra in dichloromethane (λ_{max}, nm (ϵ, M^{-1} cm^{-1})): 370 (3.5×10^4), 416 (1.84×10^4), 494 (7.9×10^3), 528 (8.4×10^3), 584 (1.1×10^4), 634 (3.35×10^4).

X-ray Data Collection. Crystals of the complexes were obtained directly from the preparations as described above. The crystals were cooled in dry ice to minimize solvent loss and immediately coated with a light hydrocarbon oil and mounted in the 90 K dinitrogen stream of a Bruker SMART 1000 diffractometer equipped with CRYO Industries low-temperature apparatus. Intensity data were collected using graphite-monochromated Mo Kα radiation. Crystal data are given in Table 4.

Solution and Structure Refinement. Scattering factors and correction for anomalous dispersion were taken from a standard source.[31] An absorption correction was applied.[32] The solution of the structure was obtained by direct methods with SHELXS-97 and subsequent cycles of least-squares refinement on F^2 with SHELXL-97.

Instrumentation. ^{1}H NMR spectra were recorded on a Bruker Avance 500 FT spectrometer (^{1}H frequency is 500.1100 MHz). The residual ^{1}H resonances of the solvent were used as a secondary chemical shift reference. The X-band EPR spectra were recorded on a Bruker ECS-106 instrument equipped with an Oxford Instruments variable-temperature liquid helium cryostat. The microwave frequency was measured by using a calibrated cavity resonator, and the magnetic field intensity was checked using solid 2,2-diphenyl-1-picrylhydrazyl as a standard.

Acknowledgment. We thank the NIH (Grant GM-26226, A.L.B.) and the NSF (Grant OSTI 97-24412) for partial funding of the 500 MHz NMR spectrometer.

Supporting Information Available: X-ray crystallographic data in CIF format. This information is available free of charge via the Internet at http://pubs.acs.org.

IC0491433

(31) *International Tables for Crystallography*; Kluwer Academic Publishers: Dordrecht, The Netherlands, 1992.
(32) Sheldrick, G. M. *SADABS*, version 2.10, 2004.